



## Estimation of Biomass Burning Emission of NO<sub>2</sub> and CO from 2019-2020 Australia Fires Based on Satellite Observations

Nenghan Wan<sup>1</sup>, Xiaozhen Xiong<sup>2</sup>, Gerard J. Kluitenberg<sup>1</sup>, J.M. Shawn Hutchinson<sup>3</sup>, Robert Aiken<sup>1</sup>, Haidong Zhao<sup>1</sup>, Xiaomao Lin<sup>1\*</sup>

5 <sup>1</sup>Department of Agronomy, Kansas Climate Center, Kansas State University, Manhattan, KS, 66502, USA

<sup>2</sup>NASA Langley Research Center, Hampton, VA, 23618, USA

<sup>3</sup>Department of Geography and Geospatial Sciences, Kansas State University, Manhattan, KS, 66502, USA

*Correspondence to:* Xiaomao Lin (xlin@ksu.edu)

10

15

20

25

30



**Abstract.** The bushfires that occurred in Australia in late 2019 and early 2020 were unprecedented in terms of their scale, intensity, and impacts. Using nitrogen dioxide (NO<sub>2</sub>) and carbon monoxide (CO) data measured by the Tropospheric Monitoring Instrument (TROPOMI), together with fire counts and fire radiative power (FRP) from MODIS, we analyzed the temporal and spatial variation of NO<sub>2</sub> and CO column densities over three selected areas covering savanna and temperate forest vegetation. The  $\Delta\text{NO}_2/\Delta\text{CO}$  emission ratio and emission factor were also estimated. The  $\Delta\text{NO}_2/\Delta\text{CO}$  emission ratio was found to be  $1.5 \pm 1.2$  for temperate forest fire and ranged from  $2 \pm 1.3$  to  $2.8 \pm 1.8$  for savanna fire. For savanna and temperate forest fires, satellited-derived NO<sub>x</sub> emission factors are  $1.29 \text{ g kg}^{-1}$  and  $1.2 \text{ g kg}^{-1}$  separately, while CO emission factors are 62.34 and 112.5  $\text{g kg}^{-1}$ . This study demonstrates that the large-scale emission ratio from the TROPOMI satellite for different biomass burnings can help identify the relative contribution of smoldering and flaming activities in a large region and their impacts on the regional atmospheric composition and air quality.

45

50

55

60



## 1 Introduction

As a consequence of climate change, extreme climatic conditions are conducive to large wildfires around the world, resulting in extensive social, economic, and environmental impacts (Bowman et al., 2017; Filkov et al., 2020). The year 2019 was the warmest and driest year on record to date in Australia (Abram et al., 2021). The high temperature aggravated the impact of low rainfall that led to low soil moisture conditions. Recently it was reported that the strong positive Indian Ocean Dipole was one of the main influences on Australia's climate in 2019 (Annual Australian Climate Statement 2019, 2022), leading to a very low rainfall across Australia. High temperatures, combined with low rainfall and high winds further exacerbated evaporative demand, resulting in canopy dieback and increasing high fire danger indices (Boer et al., 2020; Nolan et al., 2020; Abram et al., 2021). It was Australia's record-breaking temperature and extremely low precipitation in 2019 and 2020 that caused these unprecedented fire disasters (Abram et al., 2021) which also resulted in significant ecological, social, and economic impacts. These mega-fires in 2019 and 2020 burned more than 8 million hectares of vegetation including more than 70% of forests, woodlands, and shrublands, and 816 native vascular plant species across the south-east of the continent (Godfree et al., 2021). Thirty-three lives were lost and more than 3,000 homes destroyed as a direct result of the fires (Filkov et al., 2020), while approximately 417 perished and 3,151 hospitalizations occurred as a result of smoke inhalation (Borchers et al., 2020). The direct economic loss was estimated at A\$40 billion (Wilkie, 2020).

Global fire events are considered to be the largest source of global carbon emissions, especially in grasslands and savannas (44%) and woodlands (16%) (van der Werf et al., 2010). Also, the open biomass burning produced 20% of global nitrogen oxides ( $\text{NO}_x$ ) and one-third to one-half of carbon monoxide (CO) emissions (Wiedinmyer et al., 2011). The  $\text{NO}_x$  undergoes smog photochemistry and converts to Ozone ( $\text{O}_3$ ) leading to increased tropospheric  $\text{O}_3$ , whereas CO is the leading sink of the hydroxyl radical (OH) and one of the precursors to tropospheric  $\text{O}_3$  (Fowler et al., 2008). Emission ratios (ER) defined as the ratio of an excess trace gas concentration ( $\Delta X$ , i.e., the mixing ratio of species  $X$ ) and the excess concentration of a reference gas ( $\Delta Y$ ) have been widely used to characterize combustion over large fire source regions (van der Werf et al., 2017, 2020). The amount of substances emitted from the burning of a particular type of land cover depends on the fuel type and completeness of combustion, for example, a relatively large amount of  $\text{NO}_2$  is emitted during hotter and cleaner flaming combustion while a larger quantity of CO is emitted during the smoldering combustion phase. Therefore, the emission ratio metric can be considered as a proxy for combustion efficiency to distinguish flaming from smoldering combustion (Andreae and Merlet, 2001). Previous studies related to CO and  $\text{NO}_2$  emissions were reported from anthropogenic (e.g., vehicles emission in urban regions), fossil fuel (e.g., coal and gas-fired power plant), and wildfire sectors based on surface and satellite observations (Zhao et al., 2011; Kononov et al., 2016; Lama et al., 2019). Besides ER, emission factor (EF) is another widely used metric to provide emission information which is defined as the amount of gas released per kg of dry fuel burned ( $\text{g kg}^{-1}$ ). It varies greatly based on individual fire conditions and fuel types. Current estimates of EFs are primarily based on laboratory studies or field measurements in limited spatial and temporal coverage (Roberts et al., 2020; Lindaas et



95 [al., 2021](#)). Satellite remote sensing instruments can eliminate those difficulties and obtain information on emissions from  
burning conditions and fuel types over large regions. The TROPOspheric Monitoring Instrument (TROPOMI) is the satellite  
instrument onboard the Copernicus Sentinel 5 Precursor launched by the European Space Agency and the overpass time is  
about 1 PM local time ([Veeffkind et al., 2012](#)). The TROPOMI has demonstrated improved accuracy and high spatial  
resolution that facilitate investigations of trace gases from space compared to other sensors such as the Ozone Monitoring  
100 Instrument and Measurement of Pollution in the Troposphere ([van der Velde et al., 2020](#)).

Burning in Australia is responsible for 14.4% of the global annual burnt area although the land of Australia only accounts for  
6% of the Earth's land area ([Giglio et al., 2013](#)). Most of these fires occurred in the semi-arid and tropical savannas that  
cover the northern part of the continent ([Russell-smitha et al., 2007](#)), but large bushfires also occurred in the temperate  
105 forests of southeast Australia ([Cai et al., 2009](#)). Through a multiple-year surface observation, the annual pattern of some  
trace gas emissions (e.g., CO) has been identified and specific emission ratios that are based on carbon monoxide (i.e.,  
CH<sub>2</sub>O/CO, C<sub>2</sub>H<sub>2</sub>/CO, C<sub>2</sub>H<sub>6</sub>/CO) from Australian savanna fires were investigated ([Paton-Walsh et al., 2010](#); [Smith et al.,  
2014](#); [Desservettaz et al., 2017](#)). However, studies related to emissions from temperate forest fires in Australia are relatively  
seldom ([Paton-Walsh et al., 2010](#); [Possell et al., 2015](#); [Guérette et al., 2018](#)) and few studies have documented NO<sub>2</sub> and CO  
110 emissions from Australian savanna and temperate forest fires over large regions.

Therefore, the objective of this study is to characterize the emission ratio and emission factor of NO<sub>2</sub> and CO over large  
savanna and temperate forest fires in Australia in 2019 and 2020 using TROPOMI satellite observation. Our paper structure  
is as follows: Sections 2 and 3 describe the datasets and methods used. In Section 4, we report the fire intensity, and daily  
115 maximum and mean NO<sub>2</sub> and CO column densities observed over 3 months in 2019 and 2020 (i.e., 1 November 2019 to 31  
January 2020) over fire hotspot regions. The emission ratios of NO<sub>2</sub> relative to CO for savanna and temperate forest fires are  
also examined. Finally, we estimated the EF using satellite-derived NO<sub>x</sub> and CO emissions. Section 5 is a summary and  
conclusion.

## 2 Data Used

### 120 2.1 GFED4s database

The Global Fire Emission Database version 4 with small fires (GFED4s) provides global estimates of monthly and daily  
burned area, emissions, and fractional contributions of different fire types with 0.25° × 0.25° spatial resolution ([Randerson et  
al., 2012](#)). This database uses the Moderate Resolution Imaging Spectroradiometer (MODIS) Collection 5.1 MCD64A1  
burned area product and includes small fires for emission estimates ([Giglio et al., 2013](#)). Six fuel classifications are  
125 estimated using land cover type product from MODIS and the University of Maryland classification scheme in the GFED4s



database, including temperate forest, boreal forest, deforested and degraded land, peatland, agricultural waste burning, and herbaceous fuel type which is composed of shrubland, savanna and grassland (van der Werf et al., 2017). In our study, the vegetation fires that happened in Australia from November 2019 to January 2020 were classified as the savanna and temperate forest fires based on GFED4s. Highlighted in Figure 1 are the three areas of interest employed in this study. There were selected from stronger biomass burning from November 2019 to January 2020 according to Godfree et al. (2021). The three selected areas include two savanna fire areas in northwestern (Area 1) and northeastern (Area 2) Australia, as well as an area with both savanna and temperate forest fires in southeast (Area 3) Australia (Fig. 1).

## 2.2 TROPOMI CO, NO<sub>2</sub>, and aerosol layer height (ALH) data

The total column density of CO from TROPOMI was estimated from spectral radiance measurements from the shortwave to infrared spectral ranges around 2.3  $\mu\text{m}$  that are sensitive to CO absorption with a daily  $5.5 \times 7 \text{ km}^2$  resolution (Landgraf et al., 2016; Borsdorff et al., 2018). Previous studies have shown that TROPOMI was able to capture the variability of daily CO as a result of atmospheric transport of pollution (Borsdorff et al., 2018; Schneising et al., 2020). The NO<sub>2</sub> tropospheric column density is detected from TROPOMI's 405 – 465 nm wavelength bands with a  $5.5 \times 3.5 \text{ km}^2$  resolution. Although there exists a negative bias of approximately 30% in the lower tropospheric columns because of cloud pressure and the *priori* NO<sub>2</sub> profile used in air mass factor calculations (Lambert et al., 2018), it is still appropriate to use TROPOMI NO<sub>2</sub> to quantify fire burning efficiency (Lama et al., 2019; van der Velde et al., 2020). Different algorithms are used to estimate NO<sub>2</sub> and CO in TROPOMI instrument channels which also provide quality assurance values (i.e., qa\_value) to help filter raw data under unclear sky conditions and/or other problematic retrievals. In our study, we collected CO retrievals with a qa\_value larger than 0.5 and NO<sub>2</sub> retrievals with a qa\_value larger than 0.75. The CO total column density and NO<sub>2</sub> tropospheric column density were then converted to units of moles per square meter ( $\text{mol m}^{-2}$ ) and millimoles per square meter ( $\text{mmol m}^{-2}$ ), respectively. The TROPOMI also provides aerosol layer height (ALH) data that are based on the O<sub>2</sub> absorption band at near-infrared wavelengths (Graaf et al., 2019). ALH data were used to define the main vertical wind layer which was required for the emission estimation procedure described in Section 3.2. We collected ALH data with a qa\_value > 0.5 and re-sampled it to the same spatial resolutions as the CO and NO<sub>2</sub> data. All TROPOMI datasets (CO, NO<sub>2</sub>, and ALH data) from November 2019 through January 2020 were included because these three months were reported as the largest fires during the 2019/20 black summer fires in Southeast Australia (Abram et al., 2021). All data were then re-sampled to  $0.05^\circ \times 0.05^\circ$  spatial resolution through an areal weighted interpolation using the Harp package from python (Niemeijer, 2017).

## 2.3 MODIS fire radiative power (FRP) and fire events

The FRP represents the instantaneous radiative energy that is released from actively burning fires and is related to the rate of biomass combustion (Wooster et al., 2003), the emission rate of trace gases, and aerosol emissions (Kaiser et al., 2012). The MODIS instrument is onboard both the Earth Observation System Terra and Aqua satellites of the National Aeronautics and



Space Administration and measures radiance in spectral channels to detect fires at a 1 km spatial resolution (Kaufman et al., 1998). The MODIS near real-time active fire products data (MCD14DL) were used to identify fire events from November 2019 through January 2020. For each day, fire pixels (i.e.,  $1 \times 1 \text{ km}^2$  grid cells) located within a 20 km distance of one another were aggregated into a “fire event” and a rectangular polygon region with  $\pm 50$  km crosswind distance and 100 km downwind distance which is large enough to include fire pixels in the group was defined to calculate emission in Section 4.3. The fire event’s center was set as the average latitude and longitude of all fire pixels, weighted by each pixel’s FRP which is related to trace gas emission and widely used to estimate fire intensity (Wooster et al., 2003; Li et al., 2018). We retained only fire events in which the total FRP was larger than 200 megawatts ( $\text{MJ s}^{-1}$ ). It should be noted that MODIS does not provide all fire event data due to cloudy days.

## 2.4 Wind

Wind fields, which include wind speed and direction, were obtained from the hourly ERA-5 reanalysis dataset from the European Center for Medium-range Weather Forecast (ECMWF). This dataset provides meteorological variables for 37 vertical layers from 1000 hPa to 1 hPa from 1979 to the present at  $0.25^\circ \times 0.25^\circ$  horizontal resolution (Hersbac et al., 2020). We first selected ERA-5 wind data at TROPOMI overpass time (1 PM at local time) and interpolated wind fields data to produce  $0.05^\circ \times 0.05^\circ$  resolution grids. Then, the data was vertically interpolated to the averaged ALH level within each fire event. For fire events without valid ALH data, we used 850 hPa, as the average level for all selected fire events is 850 hPa.

## 3. Methods used for Calculating Emission Ratio and Emission Factor

### 3.1 Emission ratio (ER)

Excess trace species concentration ( $\Delta X$ ) is defined as the difference between concentrations of species  $X$  in the fire plume ( $X_{fire}$ ) and in the ambient background ( $X_{bg}$ ). Usually,  $\Delta X$  is divided by a reference species ( $\Delta Y$ ), such as CO or  $\text{CO}_2$ , to get the emission ratio (ER) between those two emitted compounds (i.e.,  $\Delta X/\Delta Y$ ). In our study, a similar local sampling method by van der Velde et al. (2020) was used to calculate the ER. To calculate excess gas concentration over the three selected  $10^\circ \times 10^\circ$  areas (Fig. 1), daily TROPOMI data were first re-sampled into a  $0.05^\circ \times 0.05^\circ$  spatial resolution grid. Next, co-located  $\text{NO}_2$  and CO column densities from TROPOMI were obtained from locations where  $\text{NO}_x$  and CO values were available from the GFED4s database in three selected areas (Fig. 1). The  $X_{fire}$  plume value was calculated as the average of all selected column densities. The corresponding ambient background  $X_{bg}$  value was calculated as the average of all values inside a  $5^\circ \times 5^\circ$  subregion upwind of the biomass burning region but within the three  $10^\circ \times 10^\circ$  study areas. The background subregions were determined by visual inspection through examining the predominant direction of the individual plume. Excess  $\text{NO}_2$  and CO concentration were determined from the expressions  $\Delta \text{NO}_2 = \text{NO}_{2,fire} - \text{NO}_{2,bg}$  and  $\Delta \text{CO} = \text{CO}_{fire} - \text{CO}_{bg}$ , respectively,



and the emission ratio was thus calculated as  $ER = \Delta NO_2 / \Delta CO$ . Days with inadequate data coverage (when the missing area exceeded 25% of the selected area in a single day) in either the background or study areas were removed during computation.

### 3.2 Emissions from satellite measurement and emission factor (EF)

190 In our study, we used an integrated mass enhancement method that has been used in previous studies (Mebust et al., 2011; Adams et al., 2019; Griffin et al., 2021) to estimate downwind flux. The periods from December 2018 to January 2019 were used as the background data for both CO and NO<sub>2</sub> column densities to represent emissions under fewer fire situations. To improve background robustness for daily gas column density, raw column density values that were above the 99<sup>th</sup> percentile were removed and then refilled back by using the nearest neighbouring interpolations. The daily column density was then  
195 calculated by subtracting corresponding monthly background values from raw daily column density values. Fire pixels were grouped based on distance as described in Section 2.3 and surrounding rectangles were defined. The total mass,  $m$  ( $g$ ), emitted by fires is the product of daily column density and area (Eq. 1).

$$m = VCD \cdot A, \quad (1)$$

VCD ( $mol\ m^{-2}$ ) is the daily vertical column density after subtracting background values, A is the rectangle area ( $m^2$ ). A  
200 line density derived from a plume traveling gaussian model over downwind under assumptions of constant wind without diffusion and deposition (Adams et al., 2019) is expressed as Eq. 2.

$$L(x) = L_0 \cdot e^{-kt} = L_0 \cdot e^{-\frac{x}{\tau\mu}}, \quad (2)$$

Where  $L_0$  ( $mol\ m^{-1}$ ) is the concentration over the fire center calculated by integrating VCD ( $mol\ m^{-2}$ ) from  $\pm 50$  km crosswind direction, the lifetime  $\tau$  is the inverse of reaction rate coefficient  $k$  ( $\tau = 1/k$ ),  $t$  is the time for emitted gas  
205 transport from fire center to downwind distance  $x$ .  $\mu$  is averaged wind speed at the mean ALH level in the rectangle to yield a single wind direction for the fires.  $L(x)$  ( $mol\ m^{-1}$ ) is the line density at  $x$  downwind distance. The total mass  $m$  also equals the integral of gas density from the fire center to  $x$  distance (Eq. 3).

$$m = \int_0^x L_0 \cdot e^{-\frac{x}{\tau\mu}} dx = L_0 \cdot \tau \cdot \mu \cdot \left(1 - e^{-\frac{x}{\tau\mu}}\right) = L_0 \cdot \tau \cdot \frac{x}{t} \cdot \left(1 - e^{-\frac{x}{\tau\mu}}\right), \quad (3)$$

Therefore,  $t = \frac{x}{\mu}$  is the residence time inside the areas from the fire center to downwind distance.  $L_0 x t^{-1}$  equals to the  
210 emission rate  $E$  ( $g\ s^{-1}$ ). Therefore, the relationship between total mass and the emission rate can be expressed as:

$$E = \frac{m}{\tau \left(1 - e^{-\frac{x}{\tau\mu}}\right)}, \quad (4)$$



In this study, the downwind distance  $x$  is set as 20 km ( $x_c$ ) based on previous studies (Adams et al., 2019; Griffin et al., 2021), therefore the area in Eq. 1 is the area of 20 km downwind distance. At last, we used Eq. 4 to estimate the emission rate with constant wind and estimated lifetime by using Eq. 2. Figure 2 (a) - (c) shows an example of calculating emission with a fire event that occurred in area 3 of southeastern Australia (29.2 °S, 151.5 °E) on 6 November 2019. We derived CO and NO<sub>2</sub> emission flux in  $g s^{-1}$  based on Eq. 4 and a ratio of NO<sub>2</sub>/NO<sub>x</sub> of 0.75 was used to convert NO<sub>2</sub> to NO<sub>x</sub>. Previous studies (Yurganov et al., 2011; R'Honi et al., 2013; Whitburn et al., 2015) indicated a 7-day or 14-day effective lifetime for CO, so a 7-day effective lifetime was used in our study determined through a sensitivity test discussed in section 4.3. For the short lifetime NO<sub>2</sub>, Mebust et al. (2011) assumed a 2-hour effective lifetime based on the fitted lifetimes from the OMI tropospheric NO<sub>2</sub> columns while Tanimoto et al. (2015) used 2 hours or 6 hours as the effective lifetimes. In our study, Eq. 2 was used to estimate the NO<sub>2</sub> lifetime by fitting an exponential to  $L(x)$  as a function of downwind distance and wind speed. Finally, we used the emission coefficient ( $g MJ^{-1}$ ), an energy-based coefficient, which is defined as the mass of pollutants emitted per unit of radiative energy. The emission coefficient was estimated as a slope of a linear relationship with an intercept fixed at zero between emission estimates and FRP (Vermote et al., 2009). For temperate and savanna fires, we converted regression emission coefficients to the EFs using an energy-to-mass factor of  $0.41 \pm 0.04 kg MJ^{-1}$ , which is the average of the  $0.368 \pm 0.015 kg MJ^{-1}$  and  $0.453 \pm 0.068 kg MJ^{-1}$  values found in studies (Wooster et al., 2005; Freeborn et al., 2008; Vermote et al., 2009).

## 4. Results and Discussion

### 4.1 Temporal evolution of fire intensity and total column density

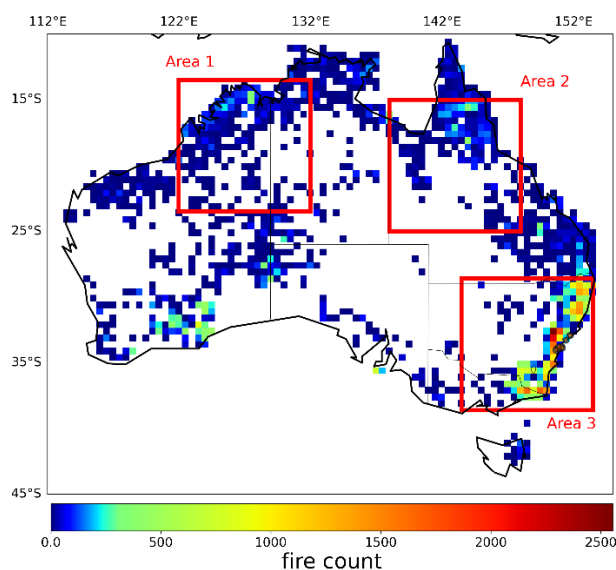






**Figure 1: Total fire counts from November 2019 to January 2020 at  $0.25^\circ \times 0.25^\circ$  resolution. Three  $10^\circ \times 10^\circ$  (latitude  $\times$  longitude) areas indicated regions of interest in this study.**

The majority of fire-affected regions during these extreme fire events were located in area 3 in southeast Australia (Fig. 1) where cumulative fire counts exceeded 1,000. Fire frequencies were much lower in areas 1 and 2 where cumulative fire counts rarely approached 250. The fire-affected areas were dominantly located either in far northern oceanic boundaries of areas 1 and 2 or in the south-eastern oceanic boundary of area 3 (Fig. 1). From fire data product of MCD14DL, the daily FRP observations showed a few distinct peaks of fire events, including three weeks from November 3<sup>rd</sup> to 25<sup>th</sup> in area 1 and a second three-week period for area 2 from December 7<sup>th</sup> to 26<sup>th</sup>. For area 3, there were two short FRP peaks in November and early January. The highest FRPs during these three months were  $4.18 \times 10^4$ ,  $3.27 \times 10^4$ ,  $9.93 \times 10^5$  MJ s<sup>-1</sup> for area 1, area 2, and area 3, respectively. The most intensive fire events in area 1 were observed in November 2019, in area 2 in December 2019, and in area 3 in January 2020 (Fig. 3). Within these three months, both NO<sub>2</sub> and CO column density distributions showed a larger mean value for each month over area 3 compared to the other two study regions (Fig. 4). These higher NO<sub>2</sub> and CO column density observations reflect the larger FRP over area 3 (Figs. 3 and 4). As expected, the daily maximum NO<sub>2</sub> column density in area 3 was nearly double that of the other two areas (Fig. 5a) but their mean values were comparable (Fig. 5c), indicating highly fluctuated NO<sub>2</sub> densities on a fire day. On the other hand, daily maximum CO column density was nearly 10 times higher in area 3 than those estimated for area 1 and area 2 (Fig. 5b), suggesting the role of different fuel and fire combustion types. The maximum daily column densities were observed as 1.1 mmol m<sup>-2</sup> for NO<sub>2</sub> and 2.3 mol m<sup>-2</sup> for CO on 4 January in area 3. For the daily mean total column densities, both NO<sub>2</sub> and CO are significantly different for all three areas under the two-sample t-test. Again, the daily mean CO was more sensitive to the FRP compared to NO<sub>2</sub> (Fig. 5d). In addition, significant increases in CO and NO<sub>2</sub> mean values in area 3 were observed in early January, which certainly was associated with the large FRP values that occurred on 30 December 2019, and 4 January 2020 (Fig. 3) by MODIS satellites.

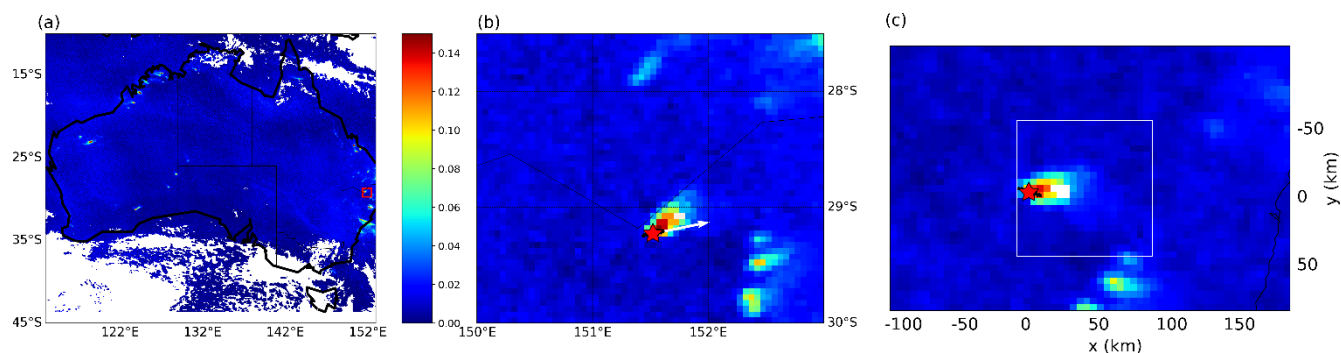
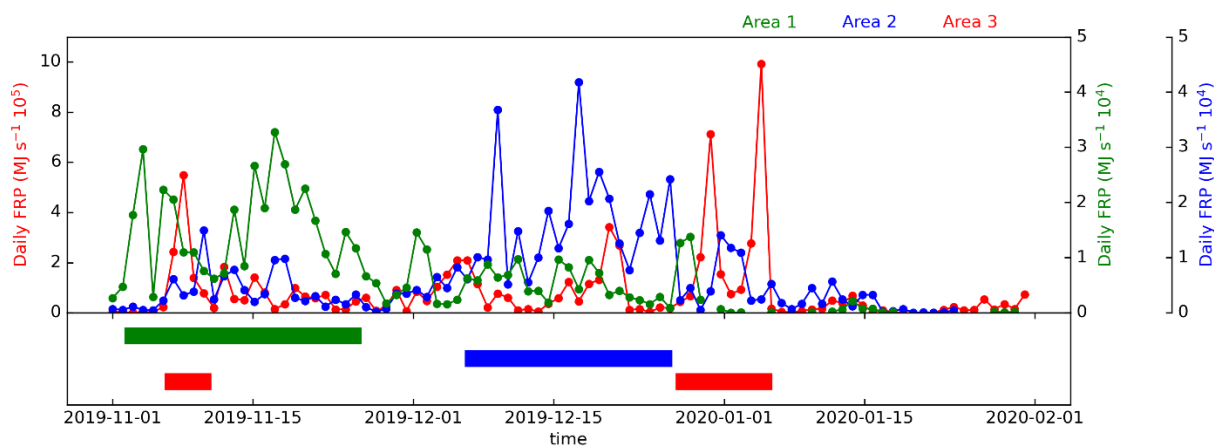


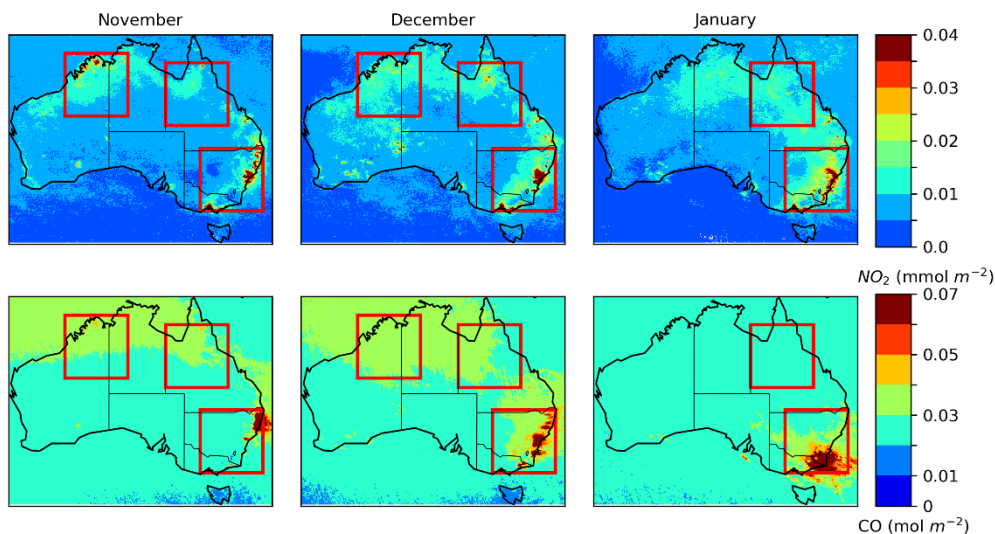
**Figure 2: An example of emission analysis for a fire event, with MODIS fire pixels indicated (black points) and the center of the fire event indicated by a red star. (a) Map of TROPOMI NO<sub>2</sub> column density over Australia on 6**



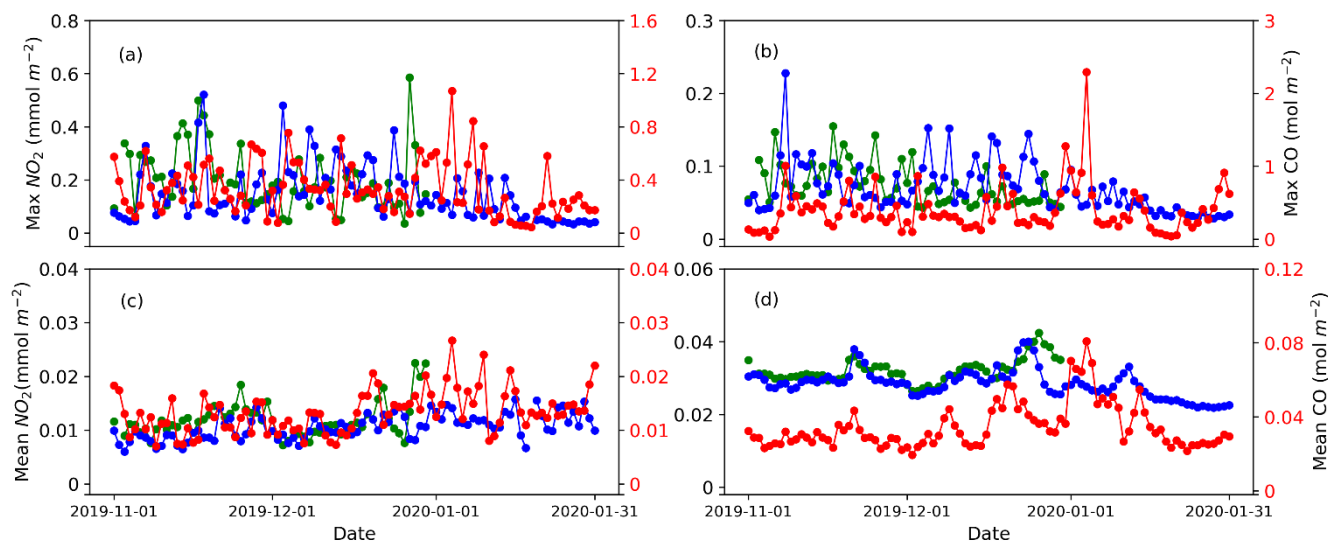
260 November 2019. The red box in southeast Australia is the fire event location. (b) The original TROPOMI NO<sub>2</sub> column density with the wind direction indicated by a white arrow. (c) The excess NO<sub>2</sub> after 1) removing background column density from original NO<sub>2</sub> and 2) rotating the entire pixels examined to align with the wind direction, thus a 20 km downwind distance area selected was used to estimate the NO<sub>2</sub> emission.



265 Figure 3: Daily fire radiative power (FRP) from November 2019 to January 2020 for area 1 (green), area 2 (blue), and area 3 (red). Several distinct periods are highlighted to show the significant increase in FRP, covering 3–25 November (area 1), 7–26 December (area 2), 7–10 November (area 3), and 29 December–5 January (area 3).



270 Figure 4: Monthly average NO<sub>2</sub> (upper panel) and CO (lower panel) column density from November 2019 to January 2020. Three 10° × 10° (latitude × longitude) areas indicated regions of interest in this study.



275 **Figure 5: Time series of daily maximum NO<sub>2</sub> (a) and CO (b) total column densities from November 2019 to January 2020 as well as daily mean NO<sub>2</sub> (c) and CO (d) for three highlighted areas: area 1 (green), area 2 (blue), and area 3 (red). Both areas 1 and 2 are displayed by the left Y axis and the area 3 are displayed by red colours of the right Y axis.**

#### 4.2 Emission ratio (ER) in savanna and temperate forest

280 Unlike directly calculating gas concentrations, the excess gas concentration (expressed as  $\Delta X$ ) removes the impact of potentially varying amounts of background concentration and thus represents the gas emissions related to fire activities. The averaged ERs derived from savanna fires were 2.3, 2.8, and 2.0 for areas 1, 2, and 3, respectively. The ER for temperate forests in area 3 was, on average, 1.5 during the three months of this study period (Fig. 6). As expected,  $\Delta NO_2$  and  $\Delta CO$  both increased with increasing FRP (high FRP periods were highlighted in Fig. 3 to correspond to points with black edge markers shown in Fig. 6) for both savanna and temperate forest-dominated landscapes, but there was a clear distinction between savanna and temperate forest fires. For the savanna fires,  $\Delta NO_2$  could approach 0.05 mmol m<sup>-2</sup> whereas changes in  $\Delta CO$  were much less at 0.03 mol m<sup>-2</sup> across all three study areas. However,  $\Delta NO_2$  (up to 0.08 mol m<sup>-2</sup>) and  $\Delta CO$  (up to 0.08 mol m<sup>-2</sup>) for temperate forest fires in area 3 were both larger in magnitude and variability.  $\Delta CO$  and  $\Delta NO_2$  emissions in temperate forest regions showed a larger enhancement compared to savanna fires. The  $\Delta NO_2$  and  $\Delta CO$  in temperate forests exceeded those in savanna fires within the same region because temperate forest fuels consisted mainly of eucalyptus trees (Godfree et al., 2021). The relatively high  $\Delta NO_2$  and small  $\Delta CO$  in the savanna portion of the three burning areas showed that the flaming combustion phase was dominant in savanna fires as this phase tends to produce higher NO<sub>2</sub> as previous research

285

290



showed (Andreae and Merlet, 2001). The day-to-day variability in  $\Delta NO_2$  was larger than  $\Delta CO$ . The  $\Delta CO$  emission ranged from 0 to  $0.08 \text{ mol m}^{-2}$  whereas  $\Delta NO_2$  emission changed from 0 to  $0.08 \text{ mmol m}^{-2}$ . Compared to van der Velde et al. (2020) who estimated  $\Delta NO_2/\Delta CO$  ERs ranged between 3.58 and 6.2 for savanna fires, the ER values in our study were lower and ranged between 2 and 2.8. The ER in temperate forest combustion reported here (1.5) was also lower than the results from Young et al. (2011), which was  $5 \pm 2 \text{ mmol mol}^{-1}$ , suggesting a complex interaction between dominant vegetation and local atmospheric turbulence during fire events. Although there are uncertainties from TROPOMI, there were distinct ERs clear resulting from savanna and temperate forest combustion (Fig. 7). This result suggests that temperate forest fires emitted larger CO per unit  $NO_2$  compared to savanna fires, indicating less efficient combustion in temperate forest fires than in savanna fires (Fig. 7).

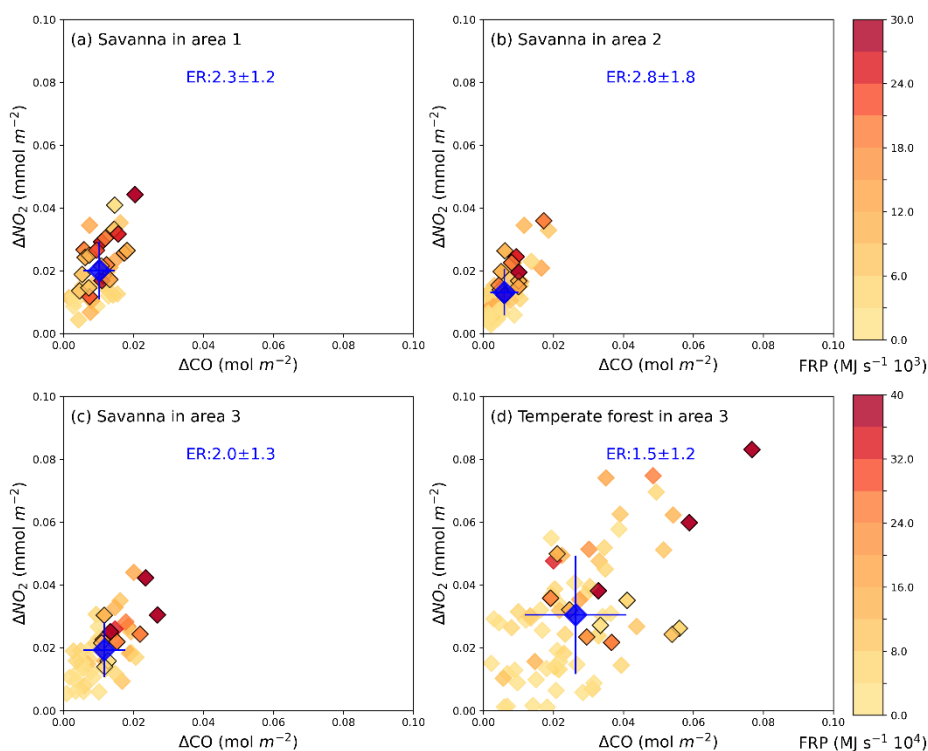


**Figure 6:** The relationship between daily  $\Delta CO$  ( $\text{mol m}^{-2}$ ) and daily  $\Delta NO_2$  ( $\text{mmol m}^{-2}$ ) in Savanna regions (a for area 1, b for area 2, and c for area 3) and temperate forest regions (d for area 3 only). The colour bars are coded by daily FRP, data points with black edges are the days with high FRP (highlighted periods) in Fig. 4. The blue markers represent the monthly average relationship between  $\Delta CO$  and  $\Delta NO_2$  with day-to-day variabilities shown represented by the error bars. ER stands for the grand emission ratio expressed by grand mean plus and minus one standard deviation.



310 One possible reason for different ER values was the different land surface sensitivities of TROPOMI in CO and NO<sub>2</sub>  
measurements (Val Martin et al., 2018; van der Velde et al., 2020). Previous studies have shown that tropospheric NO<sub>2</sub>  
measurement was less sensitive to sources in the planetary boundary layer than CO measurements, which causes the  
underestimated  $\Delta NO_2$  (Borsdorff et al., 2018; van der Velde et al., 2020). A second source is the highly reactive property of  
NO<sub>2</sub>. The short lifetime of NO<sub>2</sub> makes the daily values underestimated compared to the CO measurement which gas has a  
315 relatively long lifetime. In addition, the natural variability of atmospheric composition (e.g., tropospheric O<sub>3</sub>, water vapor)  
and different measurement techniques may contribute to the measurement uncertainty.

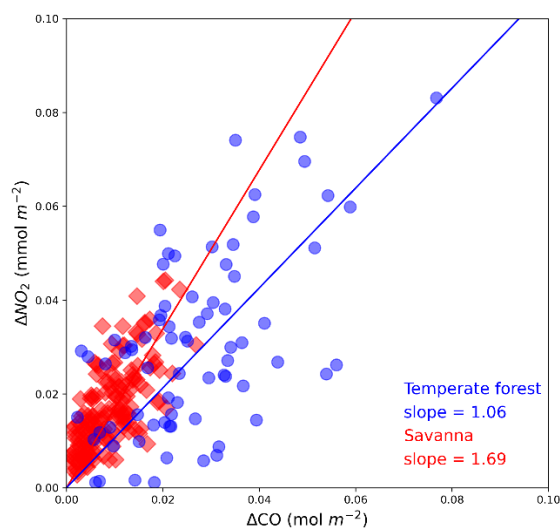


**Figure 7: The relationship between daily  $\Delta CO$  ( $\text{mol m}^{-2}$ ) and daily  $\Delta NO_2$  ( $\text{mmol m}^{-2}$ ) was derived from TROPOMI for all regions. The slope of linear fit with an intercept at zero represents the combustion efficiency of different fire types.**

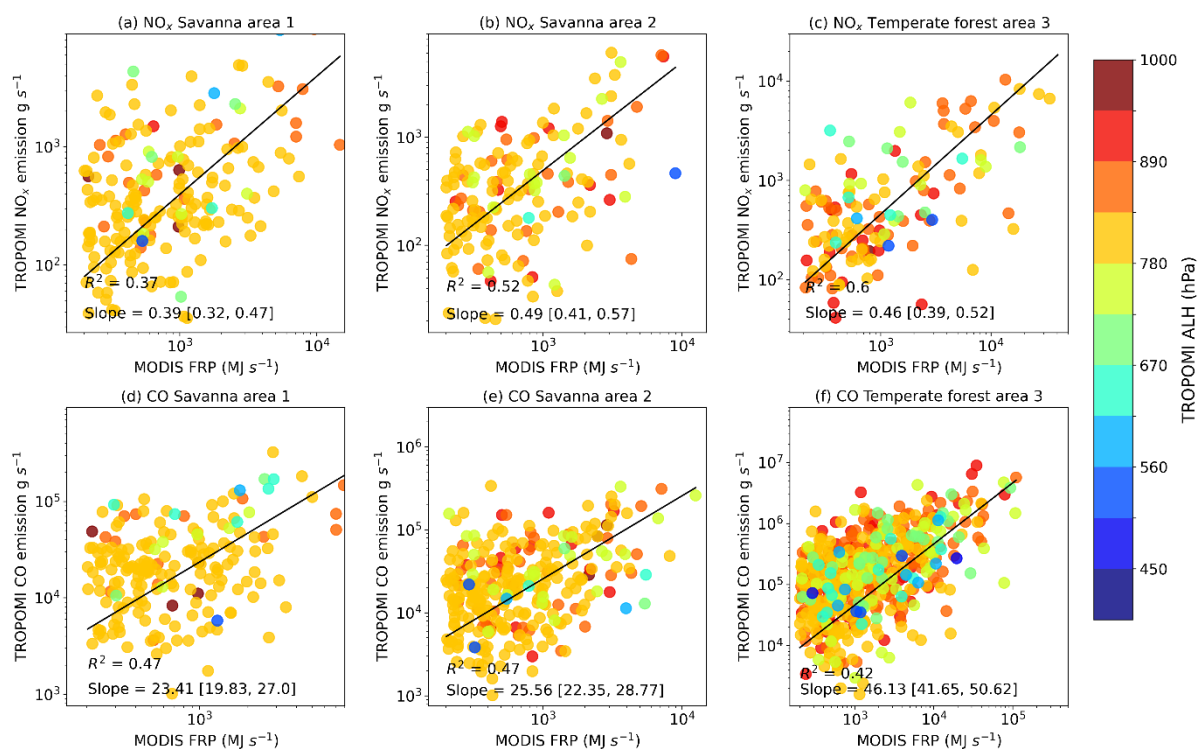
320

#### 4.3 Satellite-derived emission factor (EF)

After deriving the NO<sub>2</sub> and CO emissions for fire events, we calculated the emission coefficient ( $\text{g MJ}^{-1}$ ) using satellite-derived emissions and FRP. The 95 % confidence intervals of the slope were computed based on the student's t-distribution test. Figure 8 shows the relationship between TROPOMI-derived NO<sub>x</sub>, CO emissions and MODIS FRP for savanna and  
325 temperate forest fires in three areas. FRP explains 42% to 60% variance in NO<sub>x</sub> emissions with the highest R<sup>2</sup> in temperate fires in area 3 and lowest in savanna fires in area 1. For CO emission, FRP explained 42% to 47% variance with the highest R<sup>2</sup> in savanna fires and the lowest in temperate fires. The variability may relate to multiple uncertainties including the satellite retrieval and emission estimate approach as we discussed below. Comparing different fire types, the NO<sub>x</sub> emission coefficient in savanna fires in area 2 is the largest ( $0.53 \text{ g MJ}^{-1}$ ), with 95% confidence intervals of  $0.44 - 0.61 \text{ g MJ}^{-1}$ , CO  
330 emission coefficient in temperate forest fires in area 3 is the largest ( $57.67 \text{ g MJ}^{-1}$ ), with 95% confidence intervals of  $57.06 - 63.28 \text{ g MJ}^{-1}$ .



To compare with previous studies, we converted emission coefficients to EFs by applying a conversion factor  $K = 0.41 \text{ kg MJ}^{-1}$  (Vermote et al., 2009). For  $\text{NO}_x$ , the satellite-derived EFs range from 1 to  $1.29 \text{ g kg}^{-1}$  in savanna fires which are agreeable with previous studies ( $1.36 \text{ g kg}^{-1}$ ) in the Jin et al. (2021) using original TROPOMI  $\text{NO}_2$  data without updating a priori profile but much lower than the work in Andreae ( $2.5 \pm 1.3 \text{ g kg}^{-1}$ ) (2019) that presented the updated compilation of EFs over the past 20 years. For temperate forests, the satellite-derived  $\text{EF}_{\text{NO}_x}$  is  $1.2 \text{ g kg}^{-1}$ , which is also less than Andreae's EFs ( $3 \text{ g kg}^{-1}$ ) (2019). For CO, the satellite-derived  $\text{EF}_{\text{CO}}$  in savanna fires ranges from  $57.1$  to  $62.34 \text{ g kg}^{-1}$  and is lower than Andreae's EFs ( $69 \pm 20 \text{ g kg}^{-1}$ ) (2019) but in the range of the field measurement (ranging 15 to  $147 \text{ g/kg}$ ) from SAFIRED campaign savanna fires in Australia (Desservettaz et al., 2017) Our satellite-derived  $\text{EF}_{\text{CO}}$  in temperate forest fires is  $112.5 \text{ g kg}^{-1}$  which is close to Andreae's EFs ( $113 \pm 50 \text{ g kg}^{-1}$ ) (2019) and Guérette's field measurement (ranging 101 to  $118 \text{ g kg}^{-1}$ ) in Australia temperate forest fires (Guérette et al., 2018).



345 **Figure 8: Scatter plots of TROPOMI-derived  $\text{NO}_x$  and CO emissions ( $\text{g s}^{-1}$ ) versus MODIS FRP in Savanna regions (a, d for area 1, b, e for area 2) and temperate forest regions (c, f for area 3). The black line indicates the regression line estimated from ordinary least squares with the intercept fixed at zero. Slopes are shown with a 95% Confidence Interval. The color represents the TROPOMI ALH of the corresponding fire events. Emissions and FRP are on log scales.**





350

Our  $\text{NO}_x$  and CO EFs are smaller than previous studies, especially  $\text{EF}_{\text{NO}_x}$ . One source of this variance is because of aerosol smoke on the CO and  $\text{NO}_2$  volume column densities. Hirsch et al. (2021) found that unprecedented bushfires in Australia caused record-breaking levels of aerosols, as TROPOMI CO values were monitored using radiances in the shortwave infrared bands so that the smoke aerosol does not have a strong effect on measurements. Schneising et al. (2020) show that the uncertainty due to smoke aerosol during several Californian wildfires was about 5%. However, smoke aerosols have always affected TROPOMI  $\text{NO}_2$  observations in the ultraviolet-visible region when estimating fire emissions. Previous studies showed an implicit aerosol correction can be applied to retrieval algorithms (Griffin et al., 2021) and without this correction, a bias of more than 40% over polluted regions could be introduced (Lorente et al., 2017), suggesting that the estimated daily CO net emission was much more accurate than  $\text{NO}_2$ . The uncertainty in the satellite emission method can also cause the variance, one is the lifetime used in emission estimation. Figure 9 shows the example of fits for  $\text{NO}_2$  in area 2, and the embedded histogram shows the frequency distribution of  $\text{NO}_2$  lifetime ranging from 1 to 4 hours over all three areas. Thus, an average of 2.5 hours for  $\text{NO}_2$  selected in our computation was optimal for calculating emission. To test the uncertainty related to different lifetime choices, the Adams et al.'s (2019) test was followed. Fluxes were recalculated by replacing the default lifetime ( $\tau_{\text{NO}_2} = 2.5$  hours,  $\tau_{\text{CO}} = 7$  days) into alternate lifetimes ( $\tau_{\text{NO}_2_{\text{lower}}} = 1$  hour,  $\tau_{\text{NO}_2_{\text{upper}}} = 4$  hours, and  $\tau_{\text{CO}_{\text{lower}}} = 14$  days), then the percent difference between EFs were calculated. The largest deviation from the default settings was defined as the uncertainty (Adams et al., 2019). For CO, the uncertainty was smaller based on the 14 days lifetime (less than 1%) while the uncertainty was larger for  $\text{NO}_2$  (43% in savanna fires in area 1) based on the largest 4-hour lifetime.

365

370

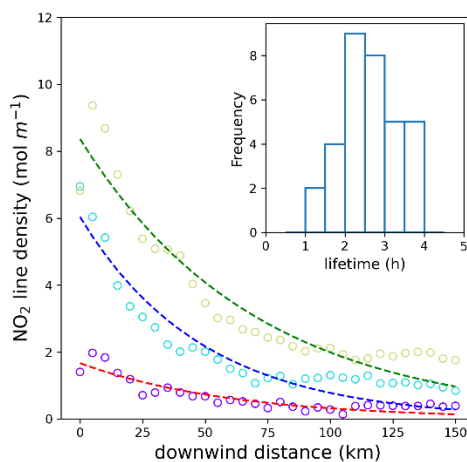


Figure 9:  $\text{NO}_2$  line density decay curves along with 150 km downwind distance in area 2. The embedded histogram shows the frequency distribution of  $\text{NO}_2$  lifetime estimated from all three areas.



## 5 Summary and Conclusions

375 The 2019-2020 black summer fires in Australia emitted large amounts of trace gases and aerosols. In this study, we focused  
on the analysis of two trace gases: CO and NO<sub>2</sub>. Based on the total columns (mean and maximum) from TROPOMI  
observations and the fire intensity from MODIS in late 2019 to early 2020, we estimated the ERs of NO<sub>2</sub> relative to CO for  
each day over three selected areas with savanna and temperate forest vegetation. For temperate forest fires, the ER was  $1.5 \pm$   
 $1.2$  which is consistent with previous studies. For savanna vegetation fires, the ER ranged from  $2 \pm 1.3$  to  $2.8 \pm 1.8$ , which  
was slightly lower compared to other studies. These differences could be traced back to different measurement techniques  
380 used, their spatial resolutions, nonlinear sensitivities to gas densities in the boundary layer, and larger NO<sub>2</sub> natural variability  
due to its short lifetime, all of which suggest that further validation of satellite products and investigations of more cases are  
required.

Using the methods from Mebust et al. (2011) and Adams et al. (2019), net emission fluxes were estimated by using a 14-day  
385 CO effective lifetime and a 2.5-hour NO<sub>2</sub> effective lifetime, and EFs were calculated. The TROPOMI-derived NO<sub>x</sub> EFs were  
 $1.29 \text{ g kg}^{-1}$  and  $1.2 \text{ g kg}^{-1}$  for savanna and temperate forest fires which are lower than previous studies while the CO EFs  
were  $62.34 \text{ g kg}^{-1}$  for savanna fires and  $112.5 \text{ g kg}^{-1}$  for the temperate forest. Our study on both savanna and temperate forest  
fire emissions demonstrates the capability and limitations of TROPOMI data for the study of the regional variability of  
combustion characteristics and their impacts on regional atmospheric composition and air quality.

390

395

400





#### 405 **Data availability**

TROPOMI CO, NO<sub>2</sub> and ALH data are available from NASA Goddard Earth Sciences (GES) Data and Information Services Center (DISC, <https://disc.gsfc.nasa.gov/datasets/>). MODIS FRP data are available from NASA Earth Data Fire Information for Resource Management Systems (<https://earthdata.nasa.gov/earth-observation-data/near-real-time/firms>). GFED4s fire emissions are available from <https://www.geo.vu.nl/~gwerf/GFED/GFED4/>. Wind data from the European Center for  
410 Medium-range Weather Forecast (ECMWF) is available at <https://cds.climate.copernicus.eu/cdsapp#!/dataset/reanalysis-era5-pressure-levels-preliminary-back-extension>

#### **Author contribution**

NW worked on the emission estimate methodology. HZ helped to interpret the satellite datasets. XX and LX conceived the  
415 structure of the paper. NW prepared the paper, and all authors contributed to the discussion and revision of the paper.

#### **Competing interests**

The authors declare that they have no conflict of interest.

#### 420 **Acknowledgments**

This study was supported in part by the U.S. Department of Agriculture, National Institute of Food and Agriculture (grant no. 2016-68007-25066). The contribution number of this manuscript is 22-275-J. We thank Dallas Staley for her outstanding contribution in editing and finalizing the paper. Her work continues to be at the highest professional level.

425

430



## References

- 435 Abram, N. J., Henley, B. J., Sen Gupta, A., Lippmann, T. J. R., Clarke, H., Dowdy, A. J., Sharples, J. J., Nolan, R. H., Zhang, T., Wooster, M. J., Wurtzel, J. B., Meissner, K. J., Pitman, A. J., Ukkola, A. M., Murphy, B. P., Tapper, N. J., and Boer, M. M.: Connections of climate change and variability to large and extreme forest fires in southeast Australia, *Commun Earth Environ*, 2, 8, <https://doi.org/10.1038/s43247-020-00065-8>, 2021.
- Adams, C., McLinden, C. A., Shephard, M. W., Dickson, N., Dammers, E., Chen, J., Makar, P., Cady-Pereira, K. E., Tam, N., Kharol, S. K., Lamsal, L. N., and Krotkov, N. A.: Satellite-derived emissions of carbon monoxide, ammonia, and nitrogen dioxide from the 2016 Horse River wildfire in the Fort McMurray area, *Atmos. Chem. Phys.*, 19, 2577–2599, <https://doi.org/10.5194/acp-19-2577-2019>, 2019.
- 440 Andreae, M. O.: Emission of trace gases and aerosols from biomass burning – an updated assessment, *Atmos. Chem. Phys.*, 19, 8523–8546, <https://doi.org/10.5194/acp-19-8523-2019>, 2019.
- Andreae, M. O. and Merlet, P.: Emission of trace gases and aerosols from biomass burning, *Global Biogeochem Cy*, 15, 955–966, <https://doi.org/10.1029/2000GB001382>, 2001.
- 445 Annual Australian Climate Statement 2019: <http://www.bom.gov.au/climate/current/annual/aus/2019/>, last access: 29 May 2022.
- Boer, M. M., Resco de Dios, V., and Bradstock, R. A.: Unprecedented burn area of Australian mega forest fires, *Nat. Clim. Change.*, 10, 171–172, <https://doi.org/10.1038/s41558-020-0716-1>, 2020.
- Borchers A., N., Palmer, A. J., Bowman, D. M., Morgan, G. G., Jalaludin, B. B., and Johnston, F. H.: Unprecedented smoke-related health burden associated with the 2019–20 bushfires in eastern Australia, *Medical Journal of Australia*, 213, 282–283, <https://doi.org/10.5694/mja2.50545>, 2020.
- 450 Borsdorff, T., aan de Brugh, J., Hu, H., Hasekamp, O., Sussmann, R., Rettinger, M., Hase, F., Gross, J., Schneider, M., Garcia, O., Stremme, W., Grutter, M., Feist, D. G., Arnold, S. G., De Mazière, M., Kumar Sha, M., Pollard, D. F., Kiel, M., Roehl, C., Wennberg, P. O., Toon, G. C., and Landgraf, J.: Mapping carbon monoxide pollution from space down to city scales with daily global coverage, *Atmos. Meas. Tech.*, 11, 5507–5518, <https://doi.org/10.5194/amt-11-5507-2018>, 2018.
- 455 Bowman, D. M. J. S., Williamson, G. J., Abatzoglou, J. T., Kolden, C. A., Cochrane, M. A., and Smith, A. M. S.: Human exposure and sensitivity to globally extreme wildfire events, *Nat Ecol Evol*, 1, 0058, <https://doi.org/10.1038/s41559-016-0058>, 2017.
- Cai, W., Cowan, T., and Raupach, M.: Positive Indian Ocean Dipole events precondition southeast Australia bushfires, *Geophys. Res. Lett.*, 36, <https://doi.org/10.1029/2009GL039902>, 2009.
- 460 Desservettaz, M., Paton-Walsh, C., Griffith, D. W. T., Kettlewell, G., Keywood, M. D., Vanderschoot, M. V., Ward, J., Mallet, M. D., Milic, A., Miljevic, B., Ristovski, Z. D., Howard, D., Edwards, G. C., and Atkinson, B.: Emission factors of trace gases and particles from tropical savanna fires in Australia, *J. Geophys. Res. Atmos.*, 122, 6059–6074, <https://doi.org/10.1002/2016JD025925>, 2017.
- 465 Filkov, A. I., Ngo, T., Matthews, S., Telfer, S., and Penman, T. D.: Impact of Australia’s catastrophic 2019/20 bushfire season on communities and environment. Retrospective analysis and current trends, *Journal of Safety Science and Resilience*, 1, 44–56, <https://doi.org/10.1016/j.jnlssr.2020.06.009>, 2020.



- Fowler, D., Amann, M., Anderson, R., Ashmore, M., Cox, P., Depledge, M., Derwent, D., Grennfelt, P., Hewitt, N., Hov, O., Jenkin, M., Kelly, F., Liss, P., Pilling, M., Pyle, J., Slingo, J., and Stevenson, D.: Ground-level ozone in the 21st century: future trends, impacts and policy implications, The Royal Society, 2008.
- 470 Freeborn, P. H., Wooster, M. J., Hao, W. M., Ryan, C. A., Nordgren, B. L., Baker, S. P., and Ichoku, C.: Relationships between energy release, fuel mass loss, and trace gas and aerosol emissions during laboratory biomass fires, *J. Geophys. Res. Atmos.*, 113, <https://doi.org/10.1029/2007JD008679>, 2008.
- Giglio, L., Randerson, J. T., and Werf, G. R. van der: Analysis of daily, monthly, and annual burned area using the fourth-generation global fire emissions database (GFED4), *J. Geophys. Res. Biogeosci.*, 118, 317–328, <https://doi.org/10.1002/jgrg.20042>, 2013.
- 475 Godfree, R. C., Knerr, N., Encinas-Viso, F., Albrecht, D., Bush, D., Christine Cargill, D., Clements, M., Gueidan, C., Guja, L. K., Harwood, T., Joseph, L., Lepschi, B., Nargar, K., Schmidt-Lebuhn, A., and Broadhurst, L. M.: Implications of the 2019–2020 megafires for the biogeography and conservation of Australian vegetation, *Nat. Commun.*, 12, 1023, <https://doi.org/10.1038/s41467-021-21266-5>, 2021.
- 480 Graaf, M. de, Haan, J. F. de, and Sanders, A. F. J.: TROPOMI ATBD of the Aerosol Layer Height, 2019.
- Griffin, D., McLinden, C. A., Dammers, E., Adams, C., Stockwell, C., Warneke, C., Bourgeois, I., Peischl, J., Ryerson, T. B., Zarzana, K. J., Rowe, J. P., Volkamer, R., Knote, C., Kille, N., Koenig, T. K., Lee, C. F., Rollins, D., Rickly, P. S., Chen, J., Fehr, L., Bourassa, A., Degenstein, D., Hayden, K., Mihele, C., Wren, S. N., Liggio, J., Akingunola, A., and Makar, P.: Biomass burning nitrogen dioxide emissions derived from space with TROPOMI: methodology and validation, *Atmos. Meas. Tech.*, <https://doi.org/10.5194/amt-2021-223>, 2021.
- 485 Guérette, E.-A., Paton-Walsh, C., Desservettaz, M., Smith, T. E. L., Volkova, L., Weston, C. J., and Meyer, C. P.: Emissions of trace gases from Australian temperate forest fires: emission factors and dependence on modified combustion efficiency, *Atmos. Chem. Phys.*, 18, 3717–3735, <https://doi.org/10.5194/acp-18-3717-2018>, 2018.
- Hersbach, H., Bell, B., Berrisford, P., Hirahara, S., Horányi, A., Muñoz-Sabater, J., Nicolas, J., Peubey, C., Radu, R., Schepers, D., Simmons, A., Soci, C., Abdalla, S., Abellan, X., Balsamo, G., Bechtold, P., Biavati, G., Bidlot, J., Bonavita, M., De Chiara, G., Dahlgren, P., Dee, D., Diamantakis, M., Dragani, R., Flemming, J., Forbes, R., Fuentes, M., Geer, A., Haimberger, L., Healy, S., Hogan, R. J., Hólm, E., Janisková, M., Keeley, S., Laloyaux, P., Lopez, P., Lupu, C., Radnoti, G., de Rosnay, P., Rozum, I., Vamborg, F., Villaume, S., and Thépaut, J.-N.: The ERA5 global reanalysis, 146, 1999–2049, <https://doi.org/10.1002/qj.3803>, 2020.
- 490 Hirsch, E. and Koren, I.: Record-breaking aerosol levels explained by smoke injection into the stratosphere, *Science*, <https://doi.org/10.1126/science.abe1415>, 2021.
- Jin, X., Zhu, Q., and Cohen, R.: Direct estimates of biomass burning NO<sub>x</sub> emissions and lifetime using daily observations from TROPOMI, *Atmos. Chem. Phys.*, <https://doi.org/10.5194/acp-2021-381>, 2021.
- 500 Kaiser, J. W., Heil, A., Andreae, M. O., Benedetti, A., Chubarova, N., Jones, L., Morcrette, J.-J., Razinger, M., Schultz, M. G., Suttie, M., and van der Werf, G. R.: Biomass burning emissions estimated with a global fire assimilation system based on observed fire radiative power, *Biogeosciences*, 9, 527–554, <https://doi.org/10.5194/bg-9-527-2012>, 2012.
- Kaufman, Y. J., Justice, C. O., Flynn, L. P., Kendall, J. D., Prins, E. M., Giglio, L., Ward, D. E., Menzel, W. P., and Setzer, A. W.: Potential global fire monitoring from EOS-MODIS, *J. Geophys. Res. Atmos.*, 103, 32215–32238, <https://doi.org/10.1029/98JD01644>, 1998.



- 505 Konovalov, I. B., Berezin, E. V., Ciais, P., Broquet, G., Zhuravlev, R. V., and Janssens-Maenhout, G.: Estimation of fossil-fuel CO<sub>2</sub> emissions using satellite measurements of “proxy” species, *Atmos. Chem. Phys.*, 16, 13509–13540, <https://doi.org/10.5194/acp-16-13509-2016>, 2016.
- Lama, S., Houweling, S., Boersma, K. F., Aben, I., van der Gon, H. A. C. D., Krol, M. C., Dolman, A. J., Borsdorff, T., and Lorente, A.: Quantifying burning efficiency in Megacities using NO<sub>2</sub>/CO ratio from the Tropospheric Monitoring Instrument (TROPOMI), *Atmos. Chem. Phys.*, <https://doi.org/10.5194/acp-2019-1112>, 2019.
- 510 Lambert, J. C., Keppens, A., Kleipool, Q., Langerock, B., Sha, M. K., Verhoelst, T., Wagner, T., Ahn, C., Argyrouli, A., and Balis, D.: S5P MPC Routine Operations Consolidated Validation Report Series. Version 12.01. 00, 2, 2018.
- Landgraf, J., aan de Brugh, J., Scheepmaker, R., Borsdorff, T., Hu, H., Houweling, S., Butz, A., Aben, I., and Hasekamp, O.: Carbon monoxide total column retrievals from TROPOMI shortwaveinfrared measurements, *Atmos. Meas. Tech.*, 9, 4955–4975, <https://doi.org/10.5194/amt-9-4955-2016>, 2016.
- 515 Li, F., Zhang, X., Kondragunta, S., and Csiszar, I.: Comparison of Fire Radiative Power Estimates From VIIRS and MODIS Observations, *J. Geophys. Res. Atmos.*, 123, 4545–4563, <https://doi.org/10.1029/2017JD027823>, 2018.
- Lindaas, J., Pollack, I. B., Garofalo, L. A., Pothier, M. A., Farmer, D. K., Kreidenweis, S. M., Campos, T. L., Flocke, F., Weinheimer, A. J., and Montzka, D. D.: Emissions of reactive nitrogen from western US wildfires during Summer 2018, *J. Geophys. Res. Atmos.*, 126, e2020JD032657, 2021.
- 520 Lorente, A., Folkert Boersma, K., Yu, H., Dörner, S., Hilboll, A., Richter, A., Liu, M., Lamsal, L. N., Barkley, M., De Smedt, I., Van Roozendaal, M., Wang, Y., Wagner, T., Beirle, S., Lin, J.-T., Krotkov, N., Stammes, P., Wang, P., Eskes, H. J., and Krol, M.: Structural uncertainty in air mass factor calculation for NO<sub>2</sub> and HCHO satellite retrievals, *Atmos. Meas. Tech.*, 10, 759–782, <https://doi.org/10.5194/amt-10-759-2017>, 2017.
- 525 Mebust, A. K., Russell, A. R., Hudman, R. C., Valin, L. C., and Cohen, R. C.: Characterization of wildfire NO<sub>x</sub> emissions using MODIS fire radiative power and OMI tropospheric NO<sub>2</sub> columns, *Atmos. Chem. Phys.*, 11, 5839–5851, <https://doi.org/10.5194/acp-11-5839-2011>, 2011.
- Niemeijer, S.: ESA Atmospheric Toolbox, in: EGU General Assembly Conference Abstracts, 8286, 2017.
- 530 Nolan, R. H., Boer, M. M., Collins, L., Dios, V. R. de, Clarke, H., Jenkins, M., Kenny, B., and Bradstock, R. A.: Causes and consequences of eastern Australia’s 2019–20 season of mega-fires, *Glob. Change Biol.*, 26, 1039–1041, <https://doi.org/10.1111/gcb.14987>, 2020.
- Paton-Walsh, C., Deutscher, N. M., Griffith, D. W. T., Forgan, B. W., Wilson, S. R., Jones, N. B., and Edwards, D. P.: Trace gas emissions from savanna fires in northern Australia, *J. Geophys. Res. Atmos.*, 115, <https://doi.org/10.1029/2009JD013309>, 2010.
- 535 Possell, M., Jenkins, M., Bell, T. L., and Adams, M. A.: Emissions from prescribed fires in temperate forest in south-east Australia: implications for carbon accounting, *Biogeosciences*, 12, 257–268, <https://doi.org/10.5194/bg-12-257-2015>, 2015.
- Randerson, J. T., Chen, Y., Werf, G. R. van der, Rogers, B. M., and Morton, D. C.: Global burned area and biomass burning emissions from small fires, *J. Geophys. Res. Biogeosci.*, 117, <https://doi.org/10.1029/2012JG002128>, 2012.
- 540 R’Honi, Y., Clarisse, L., Clerbaux, C., Hurtmans, D., Dufлот, V., Turquety, S., Ngadi, Y., and Coheur, P.-F.: Exceptional emissions of NH<sub>3</sub> and HCOOH in the 2010 Russian wildfires, *Atmos. Chem. Phys.*, 13, 4171–4181, <https://doi.org/10.5194/acp-13-4171-2013>, 2013.



- Roberts, J. M., Stockwell, C. E., Yokelson, R. J., De Gouw, J., Liu, Y., Selimovic, V., Koss, A. R., Sekimoto, K., Coggon, M. M., and Yuan, B.: The nitrogen budget of laboratory-simulated western US wildfires during the FIREX 2016 Fire Lab study, *Atmos. Chem. Phys.*, 20, 8807–8826, 2020.
- 545 Russell-Smith, J., Yates, C. P., Whitehead, P. J., Smith, R., Craig, R., Allan, G. E., Thackway, R., Frakes, I., Cridl, S., Meyer, M. C. P., Gilli, A. M., and L, D.: Bushfires ‘down under’: patterns and implications of contemporary Australian landscape burning, *Int. J. Wildland Fire*, 2007.
- Schneising, O., Buchwitz, M., Reuter, M., Bovensmann, H., and Burrows, J. P.: Severe Californian wildfires in November 2018 observed from space: the carbon monoxide perspective, *Atmos. Chem. Phys.*, 20, 3317–3332, 550 <https://doi.org/10.5194/acp-20-3317-2020>, 2020.
- Smith, T. E. L., Paton-Walsh, C., Meyer, C. P., Cook, G. D., Maier, S. W., Russell-Smith, J., Wooster, M. J., and Yates, C. P.: New emission factors for Australian vegetation fires measured using open-path Fourier transform infrared spectroscopy – Part 2: Australian tropical savanna fires, *Atmos. Chem. Phys.*, 14, 11335–11352, <https://doi.org/10.5194/acp-14-11335-2014>, 2014.
- 555 Tanimoto, H., Ikeda, K., Boersma, K. F., A, R. J. van der, and Garivait, S.: Interannual variability of nitrogen oxides emissions from boreal fires in Siberia and Alaska during 1996–2011 as observed from space, *Environ. Res. Lett.*, 10, 065004, <https://doi.org/10.1088/1748-9326/10/6/065004>, 2015.
- Val Martin, M., Kahn, R. A., and Tosca, M. G.: A Global Analysis of Wildfire Smoke Injection Heights Derived from Space-Based Multi-Angle Imaging, *Remote Sens.*, 10, 1609, <https://doi.org/10.3390/rs10101609>, 2018.
- 560 Veefkind, J. P., Aben, I., McMullan, K., Förster, H., de Vries, J., Otter, G., Claas, J., Eskes, H. J., de Haan, J. F., Kleipool, Q., van Weele, M., Hasekamp, O., Hoogeveen, R., Landgraf, J., Snel, R., Tol, P., Ingmann, P., Voors, R., Kruizinga, B., Vink, R., Visser, H., and Levelt, P. F.: TROPOMI on the ESA Sentinel-5 Precursor: A GMES mission for global observations of the atmospheric composition for climate, air quality and ozone layer applications, *Remote Sensing of Environment*, 120, 70–83, <https://doi.org/10.1016/j.rse.2011.09.027>, 2012.
- 565 van der Velde, I. R., van der Werf, G. R., Houweling, S., Eskes, H. J., Veefkind, J. P., Borsdorff, T., and Aben, I.: Biomass burning combustion efficiency observed from space using measurements of CO and NO<sub>2</sub> by TROPOMI, *Atmos. Chem. Phys.*, <https://doi.org/10.5194/acp-2020-272>, 2020.
- Vermote, E., Ellicott, E., Dubovik, O., Lapyonok, T., Chin, M., Giglio, L., and Roberts, G. J.: An approach to estimate global biomass burning emissions of organic and black carbon from MODIS fire radiative power, *J. Geophys. Res. Atmos.*, 570 114, 2009.
- van der Werf, G. R., Randerson, J. T., Giglio, L., Collatz, G. J., Mu, M., Kasibhatla, P. S., Morton, D. C., DeFries, R. S., Jin, Y., and van Leeuwen, T. T.: Global fire emissions and the contribution of deforestation, savanna, forest, agricultural, and peat fires (1997–2009), *Atmos. Chem. Phys.*, 10, 11707–11735, <https://doi.org/10.5194/acp-10-11707-2010>, 2010.
- 575 van der Werf, G. R., Randerson, J. T., Giglio, L., van Leeuwen, T. T., Chen, Y., Rogers, B. M., Mu, M., van Marle, M. J. E., Morton, D. C., Collatz, G. J., Yokelson, R. J., and Kasibhatla, P. S.: Global fire emissions estimates during 1997–2016, *Earth Syst. Sci. Data*, 9, 697–720, <https://doi.org/10.5194/essd-9-697-2017>, 2017.
- Whitburn, S., Van Damme, M., Kaiser, J. W., van der Werf, G. R., Turquety, S., Hurtmans, D., Clarisse, L., Clerbaux, C., and Coheur, P.-F.: Ammonia emissions in tropical biomass burning regions: Comparison between satellite-derived emissions and bottom-up fire inventories, *Atmospheric Environment*, 121, 42–54, <https://doi.org/10.1016/j.atmosenv.2015.03.015>, 580 2015.



- Wiedinmyer, C., Akagi, S. K., Yokelson, R. J., Emmons, L. K., Al-Saadi, J. A., Orlando, J. J., and Soja, A. J.: The Fire INventory from NCAR (FINN): a high resolution global model to estimate the emissions from open burning, *Geosci. Model Dev.*, 4, 625–641, <https://doi.org/10.5194/gmd-4-625-2011>, 2011.
- 585 Devastating bushfire season will cost Australian economy \$20BILLION, Experts Warn:  
<https://www.dailymail.co.uk/news/article-7863335/Devastating-bushfire-season-cost-Australian-economy-20BILLION-experts-warn.html>, last access: 19 August 2021.
- Wooster, M. J., Zhukov, B., and Oertel, D.: Fire radiative energy for quantitative study of biomass burning: derivation from the BIRD experimental satellite and comparison to MODIS fire products, *Remote Sens. Environ.*, 86, 83–107, [https://doi.org/10.1016/S0034-4257\(03\)00070-1](https://doi.org/10.1016/S0034-4257(03)00070-1), 2003.
- 590 Wooster, M. J., Roberts, G., Perry, G. L. W., and Kaufman, Y. J.: Retrieval of biomass combustion rates and totals from fire radiative power observations: FRP derivation and calibration relationships between biomass consumption and fire radiative energy release, *J. Geophys. Res. Atmos.*, 110, 2005.
- Young, E. and Paton-Walsh, C.: Emission Ratios of the Tropospheric Ozone Precursors Nitrogen Dioxide and Formaldehyde from Australia's Black Saturday Fires, *Atmosphere*, 2, 617–632, <https://doi.org/10.3390/atmos2040617>, 2011.
- 595 Yurganov, L. N., Rakitin, V., Dzhola, A., August, T., Fokeeva, E., George, M., Gorchakov, G., Grechko, E., Hannon, S., Karpov, A., Ott, L., Semutnikova, E., Shumsky, R., and Strow, L.: Satellite- and ground-based CO total column observations over 2010 Russian fires: accuracy of top-down estimates based on thermal IR satellite data, *Atmos. Chem. Phys.*, 11, 7925–7942, <https://doi.org/10.5194/acp-11-7925-2011>, 2011.
- 600 Zhao, Y., Nielsen, C. P., Lei, Y., McElroy, M. B., and Hao, J.: Quantifying the uncertainties of a bottom-up emission inventory of anthropogenic atmospheric pollutants in China, *Atmos. Chem. Phys.*, 11, 2295–2308, <https://doi.org/10.5194/acp-11-2295-2011>, 2011.